FISEVIER

Contents lists available at ScienceDirect

## Chemical Engineering Journal Advances

journal homepage: www.sciencedirect.com/journal/chemical-engineering-journal-advances





# Silver oxide integrated ionic polymer composite for wearable sensing and water purification

Priya Khanduri <sup>a</sup>, Varij Panwar <sup>a,\*\*</sup>, Pradeep Kumar Sharma <sup>a</sup>, Gopinathan Anoop <sup>b</sup>, Sanjeev Kumar <sup>c</sup>, Sukho Park <sup>d,\*</sup>

- a Graphic Era (Deemed to be University), Dehradun, India
- <sup>b</sup> Department of Physics, Amrita Vishwa Vidyapeetham, Amritapuri 690525, India
- <sup>c</sup> Department of Physics, Rajiv Gandhi University, Arunachal Pradesh, India
- d Department of Robotics and Mechatronics Engineering, Daegu Gyeongbuk Institute of Science and Technology (DGIST), Daegu, South Korea

#### ARTICLE INFO

#### Keywords: Ionic Polymer Composite Metal nanoparticles Wearable Sensing Water purification

#### ABSTRACT

Integrating metal nanoparticles (NPs) with ionic polymer blends/composites showed immense interest for their potential in wearable sensors, soft robotic arms, flexible man-machine interfaces of biomedical devices, and water purification applications. However, conventional NPs attached ionic polymer composites exhibit limitations such as low sensitivity ( $\Delta R/R$ ), low total dissolved solids (TDS) reduction, and low phosphate (PO4-P) removal rate. Herein, ionic polymer composites (IPCs) using flower-shaped silver oxide ( $\Delta R/R$ ) attached Poly (vinylidene fluoride) (PVDF)/ polyvinylpyrrolidone (PVP)/ionic liquid (IL) were designed and developed for wearable sensing and water purification. The IPCs demonstrated remarkably high  $\Delta R/R$  values of 50, 10, and 3.5 corresponding to the wrist movement of  $\Delta R/R$ 0, finger movement of  $\Delta R/R$ 1 and chin movements respectively. The Ag<sub>2</sub>O-based IPC recorded a significant reduction of TDS from sewage water from 3405 ppm to 1035 ppm, elevated the dissolved oxygen (DO) levels in the sewage water from 1.2 mg/l to 6.8 mg/l, and removed approximately 87.38 % phosphate from sewage water. Due to the uniform distribution of Ag<sub>2</sub>O within pores of IPC, it demonstrated enhanced performance for wearable and wastewater treatment applications.

#### 1. Introduction

Ionic polymer composites/blends have found applications across a broad spectrum of fields such as dynamic user-device interfaces [1], biomedical devices [2], sensors [3], strain gauges [4], actuators [5], and energy harvesting appliances [6]. This is primarily attributed to their high flexibility and the ease with which ions move when the samples are bent or stretched. Among these applications, piezoresistive strain sensing has gathered significant attention due to its extensive integration into our daily lives. Notably, it finds practical use in commonly encountered devices such as breathing monitors, wrist movement sensors, blood pressure monitors, smartwatches, and mobile touchscreen interfaces [6,7]. The survival and progress of human society significantly depend on water, with its demand increasing nearly six-fold over the past century [8,9]. Water scarcity persists as a global challenge, impacting billions annually, prompting significant investment in seeking viable solutions. Enhancing the efficiency and affordability of

water purification membranes has thus emerged as a crucial endeavor [10,11]. Widely used polymeric membranes are prone to fouling, especially when employed in treating surface water tainted with natural organic materials and bacteria. Surface alteration could potentially tackle this concern by providing the membrane with antifouling and antibacterial attributes [12,13].

For wearable applications, ionic polymer composites need to have high values of  $\Delta R/R$  and gauge factor (G). Various PVA-based wearable sensors such as poly(vinyl alcohol) PVA/polyelectrolytes, PVA/ionic liquids, PVA/biodegradable ionic liquids, and PVA/conducting polymer were proposed due to their biocompatible nature and hydrophilic nature [14-17]. However, PVA-based wearable sensors typically generate low sensing signals in terms of resistance and voltage [18,19]. Moreover, the PVA-based membranes lack sufficient mechanical strength for water purification.

PVDF-based ionic polymer composites/blends have proven to be highly effective, offering advantages such as excellent sensitivity, cost-

E-mail addresses: varijpanwar@geu.ac.in (V. Panwar), shpark12@dgist.ac.kr (S. Park).

https://doi.org/10.1016/j.ceja.2024.100651

 $<sup>^{\</sup>ast}$  Corresponding author.

 $<sup>^{\</sup>ast\ast}$  Co-corresponding author.

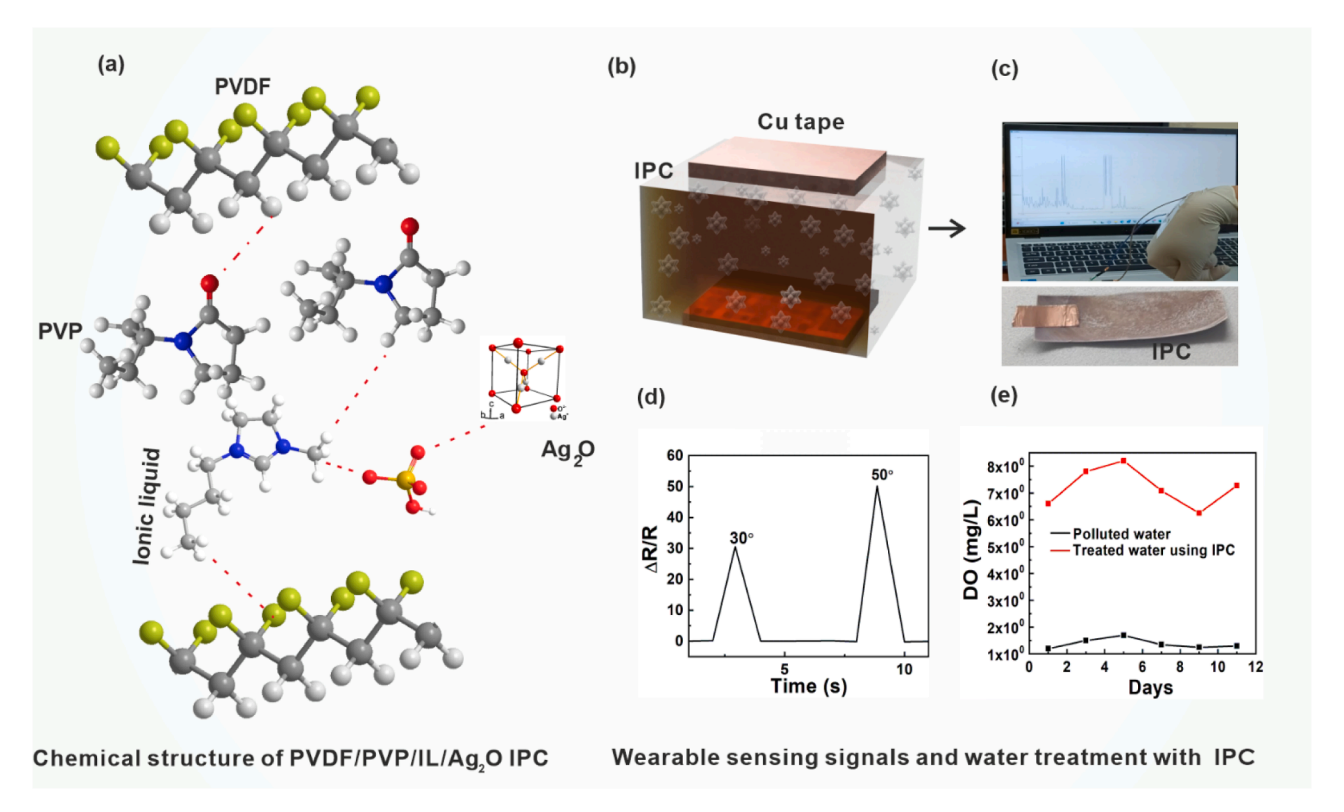


Fig. 1. (a) Chemical structure of PVDF/PVP/IL/Ag<sub>2</sub>O ionic polymer composite (IPC) membrane, (b) Skematic diagram of IPC (c) digital image of attaching IPCs on the wrist movement (d) Output sensing signals after attaching IPC on bending hand, and (e) DO of polluted and treated water using IPC with number of days.

effectiveness, versatile design options, customizable properties, remarkable mechanical flexibility, ductility in dry and wet conditions, and controllable environmental responsiveness [20-23]. Although PVDF/Ionic liquids were utilized for piezo sensing applications, they typically exhibited low gauge factor [20,24].

The charged nanofiltration membranes exhibited over 60 % TDS rejection in the power plant scrubber wastewater [25]. The PVA/cellulose acetate (CA)/polyethylene glycol (PEG) composite multilayer membrane was employed in treating brackish groundwater samples, resulting in a low TDS content of 933 mg/L [26]. When comparing the polyethersulfone (PES)/polyvinylpyrrolidone (PVP) membrane with the Ag/polydopamine (PDA)/PES/PVP membrane, the latter demonstrates an approximately 8 % and 10 % higher removal of TDS from samples taken from the river and lake water, respectively [12]. Lake water pH increased from 5.04 to 5.75 with the PES/PVP membrane and from 5.68 to 6.34 with the Ag/PDA/PES/PVP membrane while river water's pH rose to 6.46 and 5.76 with Ag/PDA/PES/ PVP and PE/PVP membranes, respectively [12]. The graphene oxide (GO)/triethylenetetramine (TETA)/copper ferrite (CuFe<sub>2</sub>O<sub>4</sub>) composite membrane outperformed the PES NF membrane, demonstrating higher removal rates for TDS at 93.8 %,  $As^{3+}$  at 81.2 %, and  $As^{5+}$  at 87.9 % [27]. The green naringin functionalized boehmite (y-AlOOH@Nar)/PVDF membranes attained elevated normalized flux and delivered substantial removal rates, including complete removal for turbidity, 89.8 % for chemical oxygen demand (COD), and moderate removal for TDS (53.0 %) [28].

Several materials have been investigated to replace traditional metal foils, including organic polymers, carbon nanotubes, graphene, bionic fibers nanowire array, and nanoparticles (NPs) [29-31]. The incorporation of NPs into the polymer solution of the examined membrane has proven successful. This approach serves to enhance various aspects of the fabricated membranes, including antifouling capabilities, morphology, mechanical properties, and overall performance. Additionally, it facilitates the creation of novel types of membranes with antibacterial properties [32-34]. The integration of metal NPs into

sensors has achieved significant success in both electrochemical and optical applications, leveraging their unique optical and electrical properties to great effect [35,36].

The advantages of flexible polymers incorporating NPs include their high conductivity, resulting in lower operation voltages, and enabling simple, rapid, and cost-effective fabrication processes. The Ag-NP formulations exhibit antimicrobial properties and can serve as highly reactive bactericidal agents, thanks to their elevated surface area [37-39]. The only disadvantage of ionic polymer-NP composites is their low gauge factor and sensitivity due to the lack of a functional group of O that reduces the reactivity and bonding of NPs with IPs.

In this study, we have developed an ionic polymer composite (IPC) employing a flower-shaped silver oxide (Ag<sub>2</sub>O) integrated with PVDF/ PVP/ionic liquid to achieve enhanced values of  $\Delta R/R$ , G, and high values of TDS reduction and PO4-P removal from sewage water. This composite holds promise for wearable device applications, particularly in the detection of breathing patterns, wrist movements, and finger gestures on the human body. In this IPC, PVDF functions as the foundational polymer, providing structural support and flexibility. PVP acts as a crosslinking agent, facilitating the attachment of sensing materials to the composite membranes. Additionally, the ionic liquid serves a dual role, acting as both a reducing agent to convert silver nitrate into silver oxide crystals and as a means to anchor these crystals within the PVDF matrix. Our developed flexible piezoresistive strain exhibits high sensitivity and is cost-effective, with fabrication techniques that are straightforward to implement. Especially, IP/0.3 shows the highest gauge factor of 888 and showed a 69.6 % decrease in TDS from sewage water. Fig. 1 (a) demonstrates the chemical structure of the PVDF/PVP/ IL/Ag<sub>2</sub>O ionic polymer composite (IPC) membrane. Fig. 1 (c) demonstrates the schematic diagram of IPC. Fig. 1 (c) demonstrates the digital image of attaching IPCs on the wrist movement. Fig. 1 (d) displays the output sensing signals after attaching IPC on the bending hand, and Fig. 1 (e) demonstrates the DO of polluted and treated water using IPC with the number of days.

Table 1
Compositions and their names.

Composition	Name
PVDF/PVP/IL with 30/15/55 ratio	IP
IP/0.3 Ag	IP/0.3 IPC
IP/0.6 Ag	IP/0.6 IPC
IP/0.9 Ag	IP/0.9 IPC

## 2. Experimental

#### 2.1. Materials

PVDF powder, possessing an average molecular weight of 534,000, was procured under the commercial name 182,702. Silver nitrate (AgNO<sub>3</sub>), ionic liquid (IL) (1-butyl-3-methylimidazolium-hydrogen sulfate), PVP, and N, N-dimethylformamide (DMF) with an average molecular weight of 236.29 and commercial name 227,056, were all supplied by Sigma-Aldrich.

#### 2.2. Fabrication process

IPCs were synthesized using a solution-casting technique. Firstly, IP was prepared using PVDF/PVP/IL with a ratio of 30/15/55, since we optimized the (P(VDF-TrFE-CTFE))/PVP/IL [40] and PVDF/PVP/polyelectrolytes ionic blend with 30/15/55 [41] ratio produced high ionic conductivity. The solutions were prepared using the different weight solute components of PVDF. To prepare the IP, the PVDF, PVP, and IL in the weight ratio of 30, 15, and 55 were dissolved in DMF and kept at a magnetic stir for 6 hours at 450 rpm. Once the solution was properly mixed, to prepare the IPC, a specific amount of AgNO3 was added, and the mixture was stirred again at 100 °C for 3 hours, resulting in a dark brown color. This brown-colored solution was then transferred to a Petri dish and heated for 8 hours at around 80 °C until the solvent fully evaporated, leaving behind a membrane. After complete evaporation, the Petri dish was allowed to cool to room temperature, and the dark brown membrane was peeled off. The dark brown color of the IPC is attributed to the presence of Ag<sub>2</sub>O. The composition of IP, various composition of IPC, and their naming are mentioned in the Table 1.

Different amounts of AgNO<sub>3</sub> (0.3 g, 0.6 g, and 0.9 g) were added to the IP, and the IL in the IP converted AgNO<sub>3</sub> into Ag<sub>2</sub>O crystals. Consequently, IP/Ag<sub>2</sub>O IPCs with three different ratios were named IP/0.3, IP/0.6, and IP/0.9 based IPCs, respectively.

## 2.3. Characterization

The structure of the IPCs was confirmed using scanning electron microscopy (SEM) and energy dispersive X-ray analysis (EDX) with a Hitachi S-4700 electron microscope. The crystalline phase of the IPCs was validated by X-ray diffraction (XRD) within the angle range of 5–90° using a Rigaku X-ray diffractometer. Fourier transform infrared (FTIR) spectroscopy, performed with a Shimadzu IR spectrometer, was used to verify the intermolecular interactions within the IPCs. The miscibility of the IPCs was assessed using a differential scanning calorimeter (DSC) at a heating rate of 5 °C/min and a nitrogen flow rate of 200 ml/min.

#### 2.4. Measurement

The dielectric constant ( $\epsilon$ ') and dielectric loss (tan $\delta$ ) of IPC were assessed utilizing an E4900A impedance analyzer (Keysight Technologies) across 20 Hz to 10 MHz frequency (f) at room temperature (25 °C).  $\epsilon$ ' was estimated as

$$\varepsilon' = (C \times l)/(A \times \varepsilon_0) \tag{1}$$

where C, l, A, and  $\varepsilon_0$  are capacitance, thickness (0.18 mm), the electrode area, and permittivity in air/free space, respectively.



Fig. 2. (a) IPC's resistance without  $\epsilon$  (b) IPC's resistance with  $\epsilon.$ 

The ionic conductivity  $\sigma_{dc}$  of the IPCs was estimated as

$$\sigma_{dc} = L/(R \times A) \tag{2}$$

where L is the sample thickness, A is the cross-sectional area and R is the composite resistance.

AC conductivity ( $\sigma_{ac}$ ) of sensors was estimated as

$$\sigma_{ac} = \omega \varepsilon_0 \ \varepsilon \ tan\delta \tag{3}$$

where  $\omega$  is the angular frequency and is calculated using the formula  $\omega = 2\pi f$ .

IPC's water uptake (WUP) indicates the proportion of water in the material and is evaluated by Eq. (4).

$$WUP = \frac{\left(W_{wet} - W_{dry}\right)}{W_{dry}} \tag{4}$$

where the weights of the wet and dried IPC are denoted by  $W_{wet}$  and  $W_{dry}$ , respectively.

The gauge factor (G) of IPC was calculated using Eq. (5) which defines the strain sensitivity of the sensor.

$$G = \Delta R(R_1 - R) / R \varepsilon \tag{5}$$

where  $\varepsilon$  is the bending strain,  $\Delta R$  represents the resistance change due to  $\varepsilon$ , R denotes the IPC's resistance without  $\varepsilon$ , R<sub>1</sub> denotes the change in IPC's resistance due to  $\varepsilon$ . This change in resistance results in a variation in the value of G. The schematic diagrams of IPCs without  $\varepsilon$  and with  $\varepsilon$  are shown in Fig. 2 (a) and Fig. 2 (b). The  $\varepsilon$  is computed using the formula 1/2r, where r is the bending radius and 1 is the thickness of the sample. The measurement setup is utilized to determine the gauge factor for measuring the data. This setup comprises a bending machine equipped with holders to secure IPC within a humidity chamber, which is connected to an STM-32 Microcontroller for measuring  $\Delta R$  and R. The data from the sample is retrieved using a data card reader. Electrical signals are captured utilizing an Arduino board with a delay of 0.5 s.

The efficacy of IPCs for sewage treatment was assessed through a 24-hour contact period with a known volume of sewage. Samples were collected before and after treatment, with subsequent analysis encompassing TDS, DO, pH,  $\sigma$ , and PO<sub>4</sub>-P.

## 3. Results and discussion

#### 3.1. Structural analysis

The crystalline structure of pure PVDF, IP, and IP/Ag<sub>2</sub>O-based IPC was investigated using XRD, and the pattern of PVDF is shown in Fig. 3 (a). The XRD pattern of PVDF exhibited reflections at 18.4° (020) and 19.7° (110), along with a moderately intense peak at 26.6 (021), indicating the presence of monoclinic  $\alpha$ -phase crystal. Fig. 3 (b) PVDF/PVP/ IL-based IP shows a single peak at 21.20° Fig. 3 (a) shows the XRD of pure PVDF, IP, IP/0.3, IP/0.6, and IP/0.9-based IPCs. The IP/0.3-based IPC shows the peaks at 20.85°, 28°, 32°, 34°, 36.5°, 45°, 55°, and 67° peaks. The peak at 20.85° implies the polarized phase ( $\beta$ ) of the PVDF in the IP/0.3 sample. The peaks at 28° (110), 32° (110), 34° (111), 36.5° (200), 55° (220), and 67° (222) are reflections from Ag<sub>2</sub>O [42-44]. The IP/0.6-based IPC shows the small and broad peaks at 21.2°, 28°, 32°, 34°, 36.5°, 45°, 55, and 67° peaks. The peak at 21.2° shows the shifting of the  $\beta$  peak of the PVDF in this sample. The broadened and small peaks

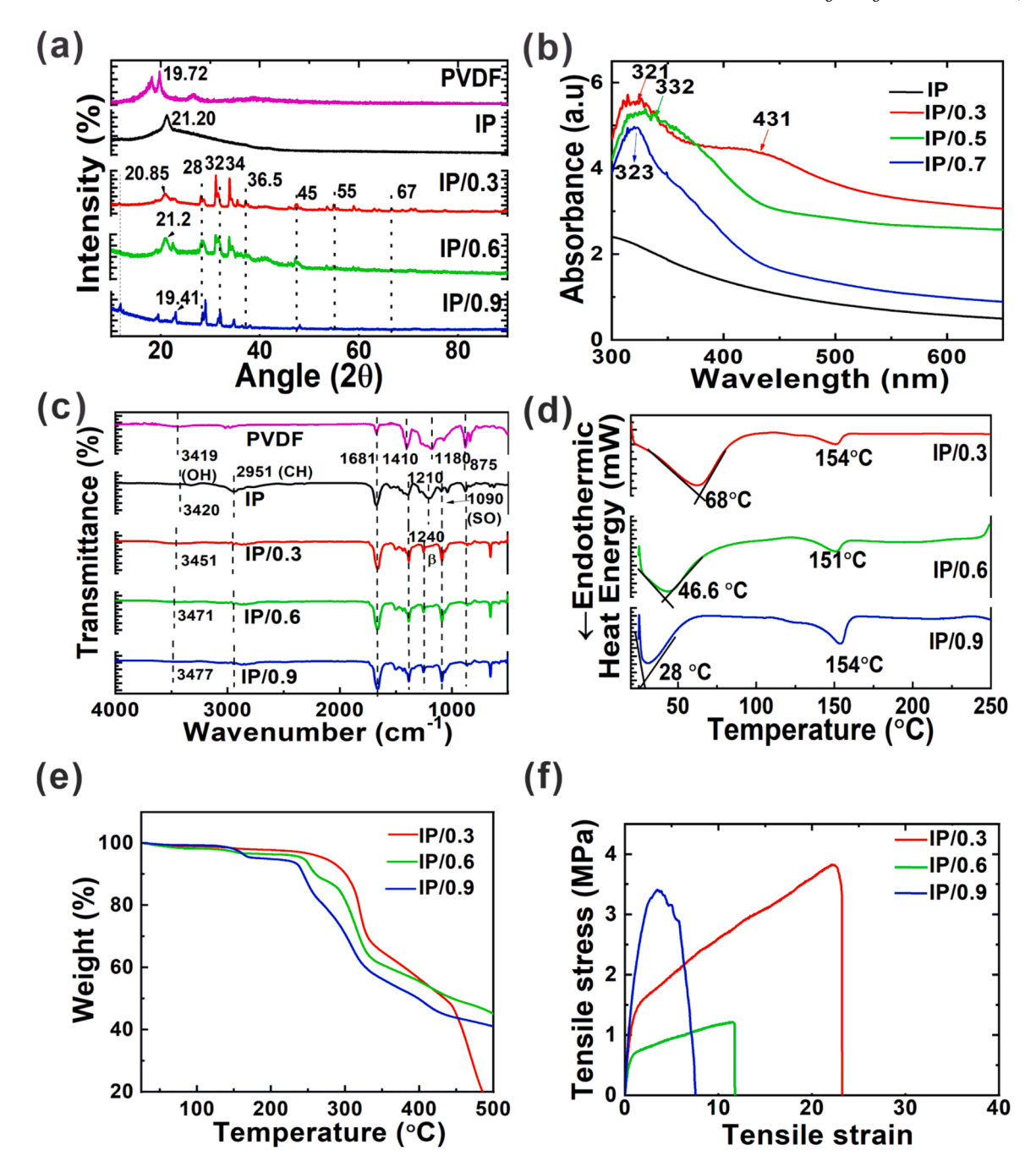


Fig. 3. (a) XRD spectra of pure PVDF and IPCs, (b) UV spectra of IPCs, (c) FTIR Spectra of pure PVDF and IPCs (d) DSC spectra of PVDF-and IPCs, (e) TGA spectra of IPCs, and (f) Tensile stress of IPCs with respect to tensile strain.

at  $28^\circ$ ,  $32^\circ$ ,  $34^\circ$ ,  $36.5^\circ$ , °55, and  $67^\circ$  demonstrate the coagulated  $Ag_2O$  crystal peaks. The IP/0.9-based IPC shows the small and broad peaks at  $19.4^\circ$ ,  $28^\circ$ ,  $32^\circ$ ,  $34^\circ$ ,  $36.5^\circ$ ,  $45^\circ$ , 55, and  $67^\circ$  The peak at  $21.2^\circ$  indicates the presence of a nonpolarized  $\alpha$  peak of the PVDF in this sample. The broadened and small peaks at  $28^\circ$ ,  $32^\circ$ ,  $34^\circ$ ,  $36.5^\circ$ , 55, and  $67^\circ$  demonstrate the  $4g_2O$  peaks. The peak around  $45^\circ$  related to the reflections from the (200) plane of metallic  $4g_2O$  The  $4g_2O$ 

The UV–Vis absorbance spectra of IP, IP/0.3, IP/0.6, and IP/0.9-based IPCs in solution form are displayed in Fig. 3 (b). The IP/0.3, IP/0.6, and IP/0.9-based IPCs, absorption peaks were observed at 321 nm,

323 nm, and 332 nm respectively, related to the absorption from  $Ag_2O$  nanoparticles (NPs peaks) [49]. The broad absorbance peak at 431 nm was also observed for the IP/0.3 IPC sample that implied the Ag NPs [50, 51]. However, in our IPC membranes,  $Ag_2O$  NPs are connected to form a flower-shaped structure.

The intermolecular bonding between AgNO $_3$ , and PVDF. PVP and IL were examined using FTIR analysis of pure PVDF, IP and IP/0.3, IP/0.6, and IP/0.9-based IPCs. The FTIR analysis of PVDF, IP, and IPC between 4000 and 500 cm<sup>-1</sup> is displayed in Fig. 3 (c). Pure PVDF show sharp peaks at 1681 cm<sup>-1</sup>,1410 cm<sup>-1</sup>, 1180 cm<sup>-1</sup>, and 876 cm<sup>-1</sup> representing the functional group G=O, C–F, C–C, and =C–H of pure PVDF, respectively [51,52]. The peak near IP shows the OH Peaks at 3420 cm<sup>-1</sup>, CH peak at 2951 cm<sup>-1</sup>, amide peak of 1681 cm<sup>-1</sup>,  $\alpha$  (nonpolar) peak of PVDF at 1210, and SO peak at 1090 cm<sup>-1</sup> are observed. The IP/0.3-based IPC

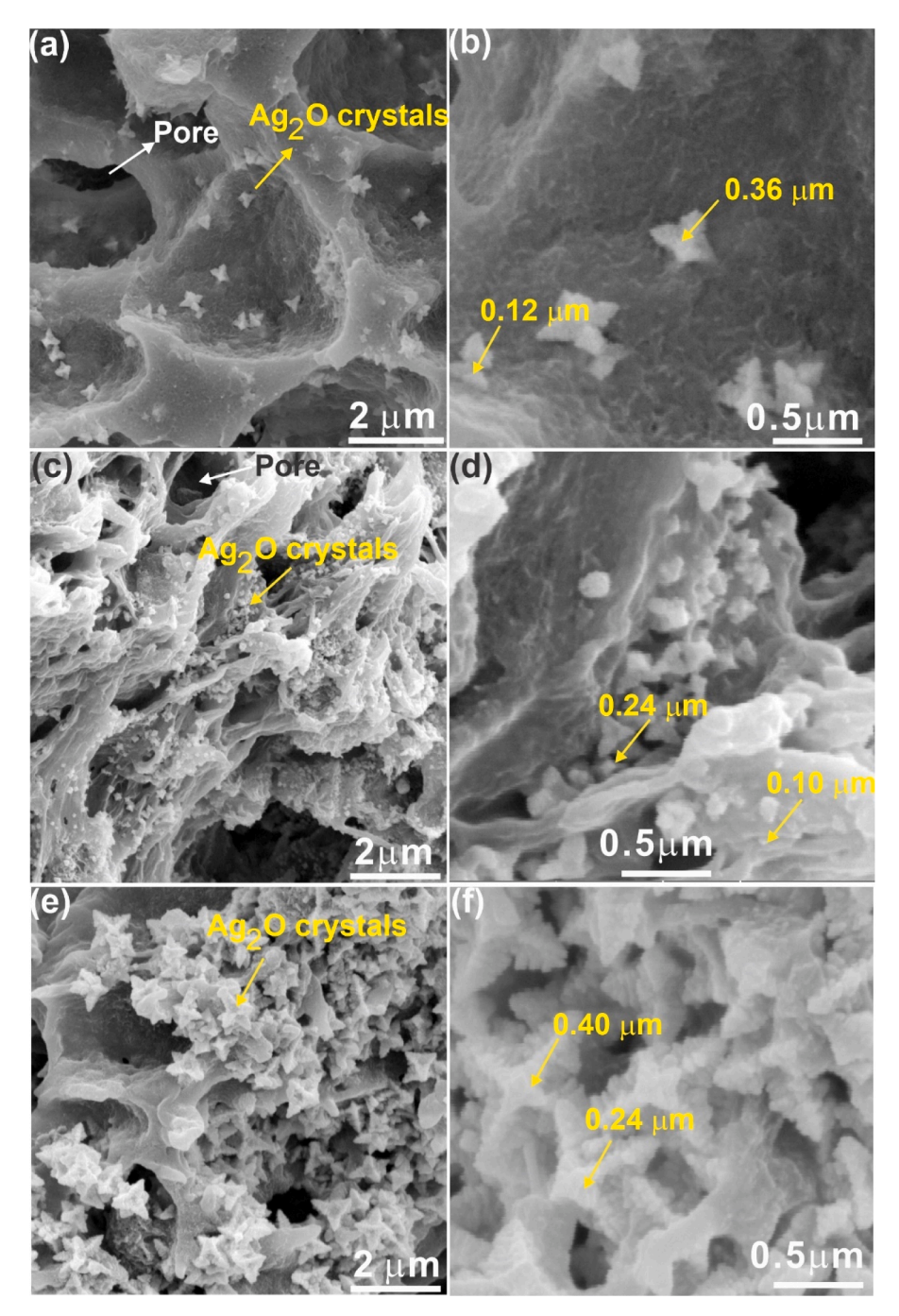


Fig. 4. SEM images of (a-b) IP/0.3, (c-d) IP /0.6, and (e-f) IP /0.9 with different magnification of 10,000x and 50,000x, respectively.

demonstrates the sharp and broad peak of OH at 3451 cm<sup>-1</sup>, amide peak of 1681, CF peak at 1410, and  $\beta$ -peak (polar phase) at 1240 are observed. The IP/0.6-based IPC demonstrates the OH peak at 3471 cm<sup>-1</sup>, amide peak of 1681, CF peak at 1410, and  $\beta$ -peak (polar phase) at 1240 are observed. The IP/0.9-based IPC demonstrates the OH peak at 3477 cm<sup>-1</sup>, amide peak of 1681, CF peak at 1410, and  $\beta$ -peak (polar phase) at 1240 are observed. The broadened and sharp peaks of OH, amide peak,  $\beta$ -peak of IP/0.3, IP/0.6, and IP/0.9-based IPCs were observed than that of the pure PVDF and IP that imply the hydrogen bonding among PVDF, PVP, IL, and AgNO<sub>3</sub>.

The amorphous and semi-crystalline nature of IPC was checked by Differential calorimetry scanning (DSC). DSC spectra of pure PVDF and IP (Fig. S1) and DSC spectra of IP/0.3, IP/0.6, and IP/0.9-based IPCs (Fig. 3 (d)) were examined to find out the melting temperature  $(T_m)$  and

glass transition ( $T_g$ ) of PVDF, IP and IPC, which reveal the chemical interaction between PVDF, PVP, IL and  $Ag_2O$  crystals. The PVDF showed only the  $T_m$  at 165 °C. IP shows the  $T_g$  and  $T_m$  at 165 °C and 165 °C, respectively. The IP/0.3, IP/0.6, and IP/0.9-based IPCs display the  $T_g$  at 68 °C, 46 °C, and 28 °C, respectively, while  $T_m$  of IP/0.3, IP/0.6, and IP/0.9-based IPCs were determined to be 154 °C, 151 °C, and 154 °C, 223 °C, respectively. The IPC shows a lower  $T_m$  than that of the pure PVDF which implies the miscibility of the. IP/0.3, IP/0.6, and IP/0.9-based IPC via hydrogen bonding between PVFD, PVP, IL, and  $Ag_2O$ . The IP/0.6-based IPC showed the lowest  $T_m$  indicating the highest miscibility and lowest resistance (see Fig. 3 (d)) among all blends.

Fig. 3 (e) displays the TGA spectra of the IP/0.3, IP/0.6, and IP/0.9-based IPCs aiming to assess their thermal stability. The first mass losses of the IP/0.3, IP/0.6, and IP/0.9-based IPCs membrane were 4 %, 3 %,

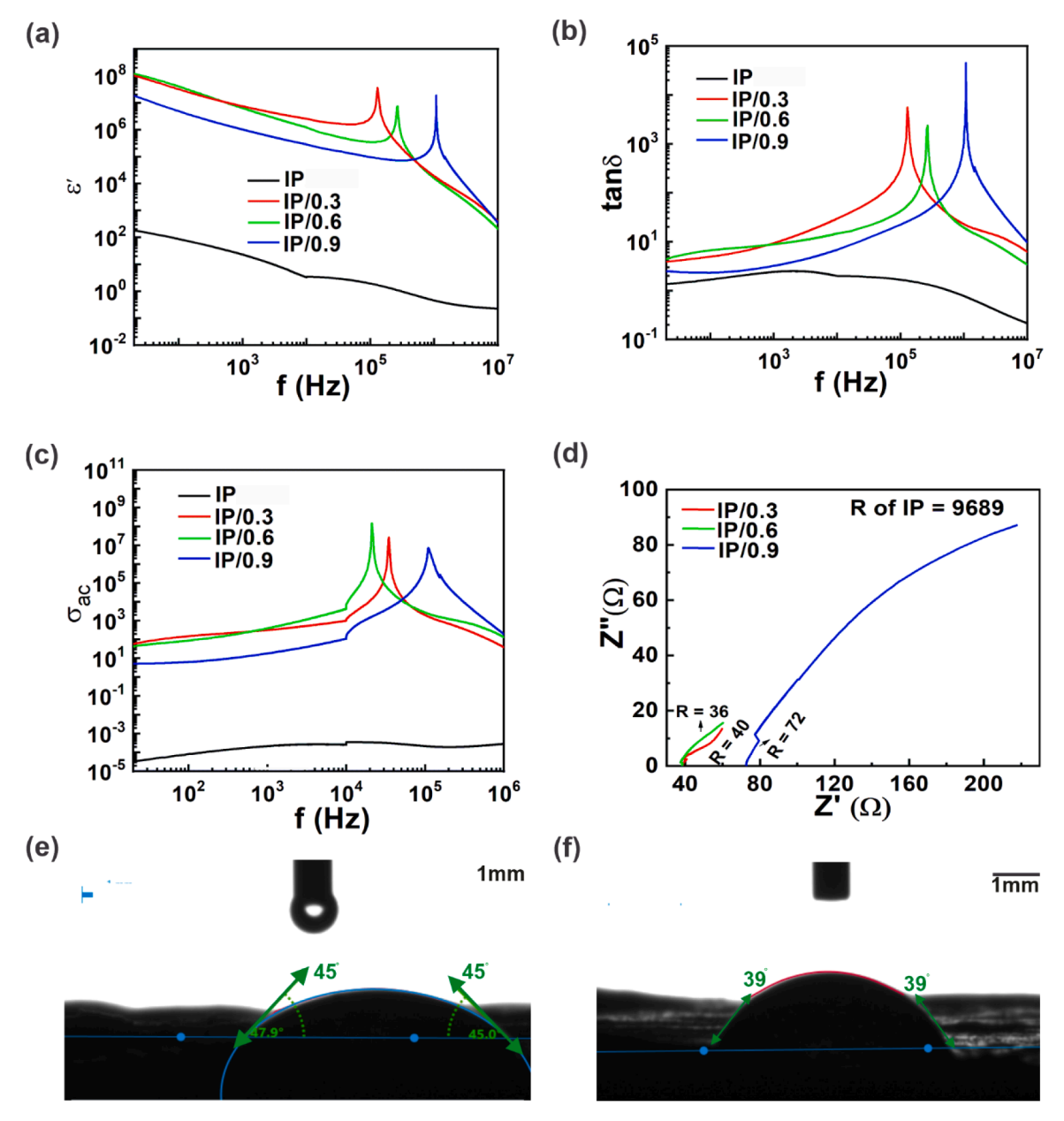


Fig. 5. (a)  $\epsilon$ ' of IPCs, (b) tan  $\delta$  of IPCs, (c)  $\sigma_{ac}$  of IPCs, and (d) Z" of IPCs s with Z', (e) Contact angle of IP/0.3, and (f) Contact angle of IP/0.6.

and 5 %, respectively, from 20 °C to 200 °C. This could be attributed to water loss from the IPCs. TGA analysis conducted on IPCs within this temperature range revealed that the IPC based on IP/0.9 absorbed a greater amount of water compared to the other two IPCs. This is further confirmed by the presence of highly hydrophilic Ag $_2$ O crystals observed in the SEM analysis. From 200 °C to 300 °C, the second mass losses of the IPC membranes based on IP/0.3, IP/0.6, and IP/0.9 were 12 %, 8 %, and 10 % respectively. This loss is attributed to the desulfonation process, indicating the incorporation of sulfonic acid groups from the acidic ionic liquid into the polymer chain of the IPCs.

The temperature ranges between 300  $^{\circ}\text{C}$  and 600  $^{\circ}\text{C}$  is attributed to the degradation of the base of the IPC membrane.

The flexibility of IPCs was examined through tensile analysis. Tensile strain, tensile stress, and Young's modulus were derived from the data presented in Fig. 3 (f) and are summarized in Table S1. Fig. 3 (f) displays the tensile stresses of the IP/0.3, IP/0.6, and IP/0.9-based IPCs with respect to tensile strain %. The IP/0.3-based IPC had a higher strain % of 22.2 than the IP/0.6, and IP/0.9-based IPCs. Every IPC showed a reduced Young's modulus, suggesting a high level of ductility. Because

of IPCs' high ductility, they can be affixed to the human body for the detection of piezoresistive signals originating from fingers and pulses.

SEM images were analyzed to examine the cross-section view of IPCs based on IP/0.3, IP/0.6, and IP/0.9 ratios, aiming to assess the dispersion, porosity, and size of Ag<sub>2</sub>O crystals within the IPC backbone. The cross-section SEM image of IP/0.3 based IPC is displayed in Fig. 4(a) and (b) with 10,000x and 50,000x magnification, respectively. The large pores (5  $\mu m$ ) were found on IPC's surface, where Ag<sub>2</sub>O crystals with flower-shaped particles were dispersed in the backbone of IPC at a 10,000x magnification. The size of Ag<sub>2</sub>O crystals was detected from 0.12μm to 0.36 μm at an increased magnification, of 50,000x. The crosssection SEM image of IP/0.6 based IPC is displayed in Fig. 4(c) and (d) with 10,000x and 50,000x magnification, respectively. The pores with dimensions from 1  $\mu m$  to 4  $\mu m$  were discovered on the cross-section view of the IPC, where flower-shaped Ag<sub>2</sub>O crystals with smaller sizes were distributed in the interfacial area of the IPC at a 10,000x magnification. The size of Ag<sub>2</sub>O crystals was detected from 0.10 µm to 0.24 µm at an increased magnification, of 50,000x. The cross-section SEM image of IP/0.9 based IPC is displayed in Fig. 4(e) and (f) with 10,000x and

 $50,\!000x$  magnification, respectively. The pore dimensions from  $1~\mu m$  were to  $3~\mu m$  discovered on the surface of the IPC, where large  $Ag_2O$  flower-shaped particles were filled in the IPC's backbone at a  $10,\!000x$  magnification. The size of  $Ag_2O$  crystals was estimated to be  $0.24~\mu m$  to  $4~\mu m$  at an increased magnification, of  $50,\!000x$ . It was reported earlier that a flower-shaped  $Ag_2O$  crystal was developed from  $AgNO_3$  using PVP and a reducing agent with a heating effect. In our case IL as a reducing agent and PVP help to develop the flower-shaped  $Ag_2O$  crystals from  $AgNO_3$  at  $80~^{\circ}C$  [53].

It was reported earlier that the flower-shaped  $Ag_2O$  crystals have a high surface-to-volume ratio [54,55] that increased the reactivity and bonding of  $Ag_2O$  crystals with IPC. The high reactivity of  $Ag_2O$ -based IPC enhanced the sensing and water purification applications. The IP/0.3 showed a uniform distribution of  $Ag_2O$  crystals than that of the IP/0.6 and IP/0.9 which is useful for high-performance wearable sensing applications.

To perform structural analysis, EDX evaluates the elemental composition analysis from IPC for various IPC compositions. Fig. S2(a) displays the cross-sectional SEM image of the IP /0.3 surface for EDX analysis, revealing the dispersion of Ag<sub>2</sub>O crystals within the large pores of IPC. The EDX spectrum of IP/0.3 (Fig. S2(b)) demonstrates the existence of C, O, Ag, S, Fe, and Mg elements. In Fig. S2(c), the SEM image of the IP/0.6 for EDX analysis reveals the attachment of coagulated Ag2O crystals to the back of the IPC surfaces. The EDX spectrum from IP /0.6 is displayed in Fig. S2 (d), proving the presence of S, C, Ag, O, Fe, and Mg elements. The IP shows higher peaks of S and Ag elements than that of the IP/0.3. Fig. S2(e) illustrates SEM images of the IP/0.9 for EDX analysis, demonstrating the presence of clustered Ag<sub>2</sub>O crystals within the IPC structure. Fig. S2(f) displays the EDX spectra of IP/0.9, which confirms the presence of C, O, S, Ag, Fe, and Mg elements. The IP/0.9 shows the highest peaks of S and Ag elements due to the large number of Ag<sub>2</sub>O crystals.

Table S2 presents the elemental compositions, both in weight (wt. percent) and atomic (wt. percent), of the surface of IP/0.3, IP/0.6, and IP/0.9 based IPC. According to Table S1 and the EDX spectra, IP/0.3 IPC comprises C, Ag, S, Mg, Fe, and O elements. The IP/0.6, and IP/0.9 comprise C, S, O, Ag, and Fe elements. The presence of additional Mg and Fe elements within the IPC may be attributed to peaks arising from potential contamination originating from the surrounding environment. The large amount of O, S, and Ag elements peaks from the IPC surface provide free ionic conduction in the IPC that helps the IPC to generate piezoresistive signals and water purification applications.

#### 3.2. Electrochemical and sensing analysis

Fig. 5(a) displays the  $\varepsilon$ ' of IPCs with frequency (f). The figure suggests that the dielectric constant ( $\varepsilon$ ') of IPCs exhibits higher values at lower frequencies, but decreases as the frequency increases, except the resonance frequency at  $1.3 \times 10^5$  Hz,  $2.5 \times 10^5$  Hz, and  $1.06 \times 10^6$  Hz for IP/0.3, IP/0.6, and IP/0.9-based IPCs. This phenomenon occurs because the dipoles of the sensors fail to align with the rapidly changing field, resulting in a decrease in the dielectric constant ( $\varepsilon$ ') at higher frequencies. All the IPCs showed higher values of  $\varepsilon$ ' than that of the pure IP due to the addition of the Ag<sub>2</sub>O crystals in IPCs. Among the IPCs examined, the IP/0.3 exhibited the highest value of  $\varepsilon$ ' in comparison to the others. Fig. 5(b) displays the  $\tan \delta$  of the IPCs as a function of frequency. The  $\tan \delta$  of IPCs initially rises as frequency (f) increases, peaking at the resonance frequency, and subsequently declines as frequency further increases. The  $\tan \delta$  of IP/0.3, IP/0.6, and IP/0.9 based IPC showed the resonance f at  $1.2 \times 10^5$  Hz,  $2.6 \times 10^5$  Hz and  $1.1 \times 10^6$  Hz

The IP/0.9-based IPC exhibits the highest  $tan~\delta$  values at high resonance frequencies, attributed to the elevated concentration of Ag<sub>2</sub>O crystals. All the IPCs showed higher values of  $tan~\delta$  than that of the pure IP due to the addition of the Ag<sub>2</sub>O crystals in IPCs.

Fig. 5(c) shows the value of  $\sigma_{ac}$  of IPCs with respect to f. The IP/0.6

**Table 2** G and  $\Delta R/R$  of different samples.

Composites	G	$\begin{array}{c} \Delta R / \\ R \end{array}$	Reference
IP	90	0.6	This work
IP/0.3 IPC	888	50	This work
IP/0.6 IPC	441	4	This work
IP/0.9 IPC	181	2.3	This work
Poly[styrene-b-(ethylene-co-butylene)-b-styrene] (SEBS)/carbon black/CNT	300	38	[56]
PVA/SCN-Ag IPNC	307	NA	[57]
PVDF/IL/CNF	4.08	4	[63]
Polyurethane/Ag flakes	229	0.8	[64]
PVA/PEDOT:PSS	396	NA	[60]
CNT/elastomeric tri-isocyanate-crosslinked polytetrahydrofuran	10 <sup>4</sup>	NA	[61]
Graphene/styrene-ethylene-butylene-styrene	120	2	[62]
Polyurethane/cellulose/silver	26	1	[63]
Ag-polytetrafluoroethylene	7.08	10	[64]
PDMS/AgNPs conductive	8.38	25	[65]

demonstrated a significantly elevated value of  $\sigma_{ac}$  when compared to the other IPCs. The value of  $\sigma_{ac}$  for IPCs exhibits a gradual increase with frequency until reaching the resonant frequency, after which it decreases. Since  $\sigma_{ac}$  is proportional to  $\varepsilon$ ',  $\tan\delta$ , and f, the  $\sigma_{ac}$  of all IPCs all show identical behavior with f as  $\tan\delta$  behaves with f. The  $\sigma_{ac}$  of IP/0.3, IP/0.6, and IP/0.9-based IPCs show resonance f at  $1.3\times10^5$  Hz,  $2.5\times10^5$  Hz and  $1.06\times10^6$  Hz p.

The IP/0.3-based IPC achieved its maximum value of  $\sigma_{ac}$  at a certain frequency. The ionic conductivity of IPCs was assessed in a hydrated state through the Nyquist plot, which represents the spectrum from imaginary (Z") to real impedance (Z'), as illustrated in Fig. 5(d). The membrane's ionic resistance (R) is identified by the point where the Z" and Z' plots intersect on the Z' axis. The R-value of IP was evaluated to be 9687 and is also stated in Fig. 5(d). The Nyquist plot of the IP/0.3, IP/ 0.6, and IP/0.9-based IPC is displayed in Fig. 4(d). R of IP/0.3, IP/0.6, and IP/0.9-based IPC was found to be 40, 36, and 72, respectively. From the spectra, the IP/0.6 yielded the minimum value of R. Table S3 shows the ionic conductivity of the IPC. The ionic conductivity of IP, IP/0.3, IP/0.6, and IP/0.9-based IPC were estimated to be 5.9  $\times$  10<sup>-5</sup>, 1.4  $\times$  $10^{-2}$ ,  $1.5 \times 10^{-2}$ , and  $7.9 \times 10^{-3}$ , respectively. The IP/0.6 exhibits the highest conductivity of 1.5  $\times$  10<sup>-2</sup> S/cm. The ionic conductivity of the IP/0.6 is shown to be 254 times greater than that of the IP. The enhanced conductivity observed in IP/0.6 was attributed to the uniform dispersion of smaller particles (0.10  $\mu m$  to 24  $\mu m$ )) of Ag<sub>2</sub>O crystals in the interfacial region of IP that will be responsible for enhanced conduction in IP/0.6, among all IPCs.

The ionic conductivity of the IP/0.6-based IPC is shown to be 254 times greater than that of the IP. The enhanced conductivity observed in IP/0.6-based IPC was attributed to the uniform dispersion of smaller particles (0.10  $\mu m$  to 24  $\mu m$ )) of  $Ag_2O$  crystals in the interfacial region of IP, low conduct angle, and optimized WUP that will be responsible for enhanced conduction in IP/0.6, among all IPCs.

The contact angle measurement was employed to assess the hydrophilic nature of the IP/0.3, IP/0.6, and IP/0.9-based IPC. A surface exhibiting a contact angle below 90° is referred to as hydrophilic. Fig. 5 (e) and (f) demonstrate the contact angles of 45° and 39° which are IP/0.3 and IP/0.6 IPC respectively. The IP/0.9 based IPC demonstrates the contact angle of 36° as shown in Fig. S4. All the samples of IPCs display a hydrophilic nature. The IP/0.9-based IPC displays the lowest contact angle of 36° compared to both the IP/0.3 and the IP/0.6 configurations. It implies that the hydrophilic nature of IPC increased with the addition of Ag<sub>2</sub>O crystals.

The appropriate amount of the WUP of IPC is required for ions to travel in IPC. Too low and too high WUP decrease the ionic conduction. The WUP of IPC is depicted in Table S3. The IP/0.9 IPC a has a high WUP among all blends; this might be due to the high hydrophilic nature of the

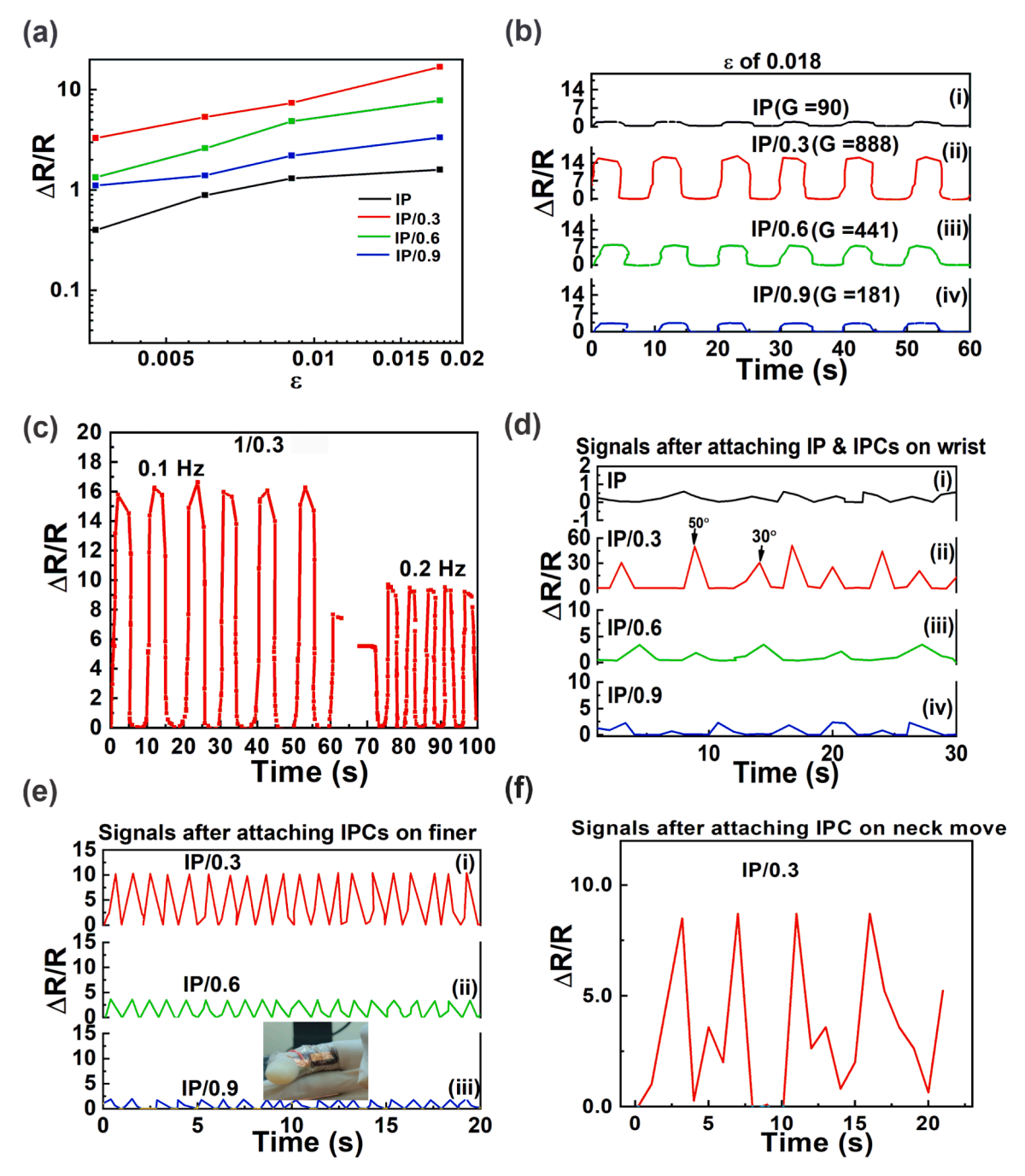


Fig. 6. (a)  $\Delta$ R/R of various IPCs with  $\epsilon$ , (b) Sensing resistance of various IPCs with a  $\epsilon$  of 0.018 at a different frequency, (c)  $\Delta$ R/R of, IP/0.3 based IPC at 0.1 Hz & 0.2 Hz frequency, (d) Sensing resistance of various IPCs by motion on wrist, (e) Sensing resistance of various IPCs by movement of finger, and (f) Sensing resistance of IP/0.3 based IPC by variation in neck movement.

Ag<sub>2</sub>O crystals which shows the lowest contact angle.

## 3.3. Piezoresistive and wearable sensing analysis

The piezoresistive sensing properties of IP/0, IP/0.3, IP/0.6, and IP/0.9-based IPCs were examined concerning the application of bending strain, focusing on parameters such as  $\Delta R/R$  and G.

The piezoresistive characteristics of IPCs were examined under a BS of 0.018 (equivalent to a bending radius of 5 mm) at 0.1 Hz frequency, as outlined in Table 2. The IP/0.3-based IPC showed larger  $\Delta$ R/R (16) and G (888) than the other IP/0, IP/0.6, and IP/0.9.

The highest sensitivity ( $\Delta R/R$ ) was attained at a BS of 0.018. Fig. 6(a) illustrates the sensing resistance of IPCs with compositions IP, IP/0.3,

IP/0.6, and IP/0.9 under a BS of 0.018 at frequencies of 0.1 Hz and 0.2 Hz. Compared to the IP/0, IP/0.6, and IP/0.9, the IP/0.3-based IPC exhibited the utmost sensitivity ( $\Delta$ R/R) and G. Fig. 6(b) displays  $\Delta$ R/R of various IP/0, IP/0.3, IP/0.6 and IP/0.9 with time at BS of 0.018. The  $\Delta$ R/R of IP/0, IP/0.3, IP/0.6, and IP/0.9 are found to be 2, 16, 8, and 3.76, respectively at BS of 0.018. The values of G of IP/0, IP/0.3, IP/0.6, and IP/0.9 are found to be 90, 888, 4,41, and 181, respectively at BS of 0.018. Fig. 6(c) displays the  $\Delta$ R/R of IP/0.3 with time at a frequency of 0.1 and 0.2 Hz under a bending radius of 0.018. The IPC shows high values of piezoresistive signals at lower f of 0.1 Hz because at lower f, ions follow the input bending cycle, and ions don't follow the bending cycle at higher f.

For wearable sensing performance, the  $\Delta R/R$  of IPCs was checked

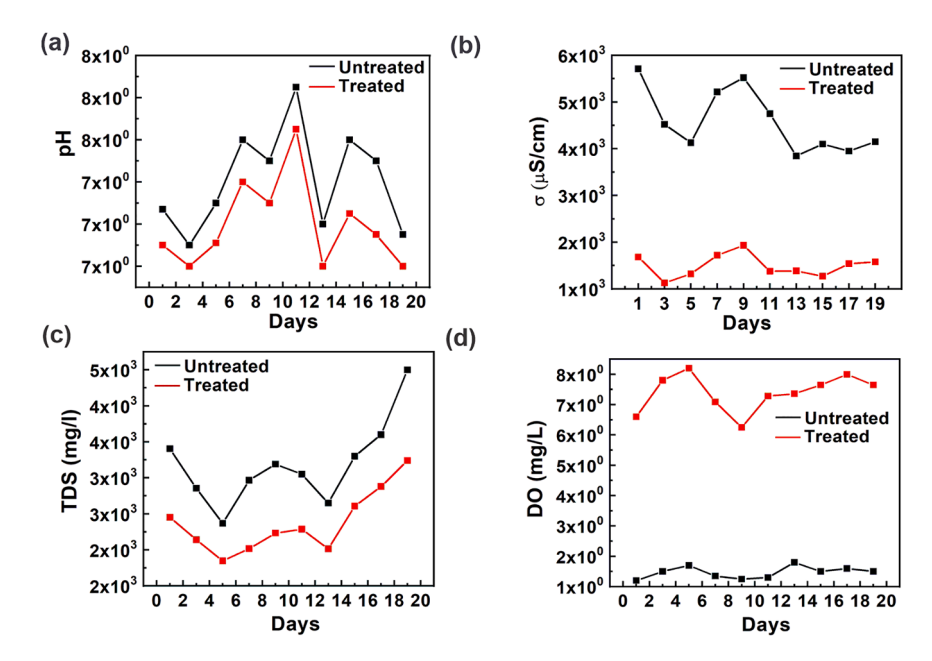


Fig. 7. (a) pH, (b) σ, (c) TDS, and (d) DO of sewage water by days for untreated and treated sewage water samples using 1/0.3 IPC, respectively.

after attaching IPCs on the wrist movement, finger movement, and breathing signals with the neck. The  $\Delta R/R$  of IP/0, IP/0.3, IP/0.6, and IP/0.9 were checked after attaching IPCs on the wrist movement of 30 ° and 50 ° and displayed in Fig. 6(d). The values of  $\Delta R/R$  of IP, IP/0.3, IP/0.6, and IP/0.9 are found to be 0.6, 50, 3, 97, and 2.3, respectively with wrist movement of 50 °. The values of  $\Delta R/R$  of IP/0, IP/0.3, IP/0.6, and IP/0.9 are found to be 0.3, 30, 2, and 0.76, respectively with wrist movement of 30 °.

Fig. 6(e) displays the variation of sensing  $\Delta R/R$  of IPCs with time after attaching IPCs on finger bending of  $180^{\circ}$ . The values of  $\Delta R/R$  of IP/0, IP/0.3, IP/0.6, and IP/0.9 are found to be 10, 50, 3.97, and 2.3, respectively with fingers. The digital image of the sample on a finger is displayed in the inset of Fig. 6 (e).

The movement examination also involved positioning 0.3-based IPC on the neck, while monitoring the sensing resistance through movements of tilting the chin downward and upward. Fig. 5(f) illustrates how the sensing  $\Delta R/R$  varies in chin-up and chin-down positions. The  $\Delta R/R$  of the IP/0.3 based IPC was observed to be 10 when the chin was positioned downward. When the chin was raised, the  $\Delta R/R$  of the IP/0.3 based IPC was measured at 3.5.

As observed from Table 2 and Fig. 6, the IP/0.3 based IPC generated high value of  $\Delta R/R$  of 50 that is higher than that of the existing Poly [styrene-b-(ethylene-co-butylene)-b-styrene] (SEBS)/carbon black/CNT [56], PVA/SCN-Ag IPNC [57], PVDF/IL/CNF [58], Polyurethane/Ag flakes [59], PVA/PEDOT:PSSA [60], CNT/elastomeric tri-isocyanate-crosslinked polytetrahydrofuran [61], Graphene/styrene—ethylene—butylene—styrene [62], polyurethane/cellulose/silver [63], Ag-polytetrafluoroethylene [64], and PDMS/AgNPs [65] conductive composites due to the highly reactive flower shaped Ag<sub>2</sub>O. The IP/0.3 showed a higher value of G than existing composites except for the CNT/elastomeric tri-isocyanate-crosslinked polytetrahydrofuran composite.

## 3.4. Water purification

The sewage water treatment was carried out using IP/0.3-based IPC. The sewage water samples were collected before and after treatment with IPC, with subsequent analysis encompassing the  $\sigma$ , TDS, DO, and pH. Fig. 7 (a), (b), (c), and (d) show the pH,  $\sigma_{dc}$ , TDS, and DO of the untreated and treated sewage water samples, respectively. The pH showed a decrease from 7.27 to 2.67, and  $\sigma_{dc}$  decreased from 5.708 mS

**Table 3**Change in DO concentration in sewage by different IPCs.

Composites	DO (mg/l)	Reference	
	Untreated Sewage	Treated Sewage	_
IP	1.3	2.9	This work
IP/0.3 IPC	1.3	6.8	This work
IP/0.6	1.3	6.2	This work
IP/0.9	1.3	5.8	This work
Electrically-induced membrane bioreactor	NA	0.1–2.5	[66]
Polyhydroxybutyrate (PHB)	NA	4	[79]
Sponge granular activated carbon MBR	NA	1–4	[67]
Oxygen-based membrane biofilm reactor	NA	0.4	[68]
Biological-band and			
suspended-honeycomb carriers MBR	NA	4	[69]
Bacillus subtilis	NA	5.7	[70]

cm $^{-1}$  to 1.682 ms cm $^{-1}$ , signifying a decrease in dissolved salts. The TDS recorded a prominent reduction from 3405 ppm to 1035 ppm, indicating a 69.6 % decrease. The DO levels in the sewage rose from 1.3 mg/l to 3.8 mg/l, confirming enhanced aerobic conditions post-treatment with the flower-shaped Ag<sub>2</sub>O attached IPC. Table S4 shows the pH and  $\sigma_{dc}$  of different IPCs. The  $\sigma_{dc}$  of IP, IP/0.6, and IP/0.9 decreased from 5.708 ms cm $^{-1}$  to 3.72 ms cm $^{-1}$ , 1.25 ms cm $^{-1}$ , and 1.71 ms cm $^{-1}$  respectively. The reduction of pH in sewage water by an IPC membrane can primarily be attributed to the acidic properties of the ionic liquid. These components release protons into the water, thus lowering the pH. The IP/0.6 membrane adsorbs the precipitation of acidic compounds present in sewage water, effectively removing these acids from the water phase and increasing the pH. The  $\sigma_{dc}$  of IP, IP/0.6, and IP/0.9 decreased from 5.708 ms cm $^{-1}$  to 3.72 ms cm $^{-1}$ , 1.25 ms cm $^{-1}$ , and an1.71 ms cm $^{-1}$ , respectively.

Table 3 shows the change in DO concentration in sewage by different IPCs. The DO of IP, IP/0.6, and IP/0.9 increased from 1.3 mg/l to 2.9 mg/l, 3.2 mg/l, and 3.4 mg/l respectively. This increase in DO levels may be attributed to various mechanisms, including catalytic oxidation, redox reactions, and photochemical reactions facilitated by silver ions,

**Table 4**TDS of different IPCs.

Composites	TDS(ppm)		Reference
	Untreated	Treated	
IP	3405	2325	This work
IP/0.3	3405	1035	This work
IP/0.6	3405	1378	This work
IP/0.9	3405	1523	This work
ED stack equipped with Neosepta ACS and CMX membranes	4567.6	826.34	[71]
PVDF/PVP membrane	833	$1820 \pm \\190$	[72]
NF-90 membranes	$5520 \pm 718$	566	[73]
Modified PVDF membranes	157,000	153,000	[74]

**Table 5** PO<sub>4</sub>-P removal rate of different IPCs.

Composites	PO <sub>4</sub> -P		PO <sub>4</sub> -P	Reference
	Untreated Sewage	Treated Sewage	removal rate (%)	
IP	6.5	4.5	30.76	This work
IP/0.3	6.5	0.72	88.92	This work
IP/0.6	6.5	1.01	84.43	This work
IP/0.9	6.5	2.17	66.61	This work
TiO <sub>2</sub> ceramic membranes	NA	NA	41	[75]
Alumina (Al <sub>2</sub> O <sub>3</sub> ) membranes	NA	NA	85	[76]
Zr-modified-	NA	NA	91.5	[77]
bentonite filled polyvinyl chloride membrane				
CMS-800	NA	NA	50.92	[78]

resulting in the creation of reactive oxygen species (ROS). These ROS contribute to the breakdown of organic matter, resulting in an overall enhancement of dissolved oxygen levels in the sewage In Table 3, an analysis of the IPCs is compared with DO data of existing membranes such as electrically-induced membrane bioreactor [66], polyhydropolyhydroxy butyrateonge granular activated carbon [67], oxygen-based membrane biofilm reactor [68], Biological-band and suspended-honeycomb carriers [69], and bacillus subtilis [70]. From this table, it was found that our IPC shows comparable results with the existing membranes.

Table 4 shows the TDS of different IPCs and the TDS data of membranes reported by other groups. The TDS of IP, IP/0.6, and IP/0.9 decreased from 3405 ppm to 2325 ppm, 1378 ppm, and 1523 respectively. Increased DO levels support the growth and activity of aerobic bacteria. The breakdown of organic matter by these microorganisms can reduce the concentration of dissolved organic compounds, thus contributing to a lower TDS. In Table 4, the TDS of IPCs is compared with various existing membranes such as ED stack equipped with Neosepta ACS and CMX membranes [71], PVDF/PVP [72], NF-90 membranes [73], and PVDF-modified membranes [74]. From the TDS data analysis, IPC showed higher TDS reduction as compared to the other existing polymer membranes, except the modified PVDF membrane due to the flower-shaped Ag<sub>2</sub>O attached IPC.

Table 5 shows the PO<sub>4</sub>-P removal rate of different IPCs. As sewage water passes through the membrane, PO<sub>4</sub>-P –bound particulates are retained by the porous structure of IPC. IP/0.3 shows highest phosphate removal (88.92 %) from sewage water as compared to other IPCs because of large pores found on the surface as shown in SEM image (Fig. 3). In Table 5, the PO<sub>4</sub>-P of IPCs showed comparable values with various existing membranes such as  $TiO_2$  ceramic membranes [75], Alumina (Al<sub>2</sub>O<sub>3</sub>) membranes [76], Zr-modified-bentonite filled polyvinyl chloride membrane [77], and CMS-800 [78].

#### 4. Conclusion

In this paper, the flower-shaped Ag<sub>2</sub>O attached IPC was designed for wearable sensing and wastewater treatment applications. The IP/0.3based IPC generated a high value of  $\Delta R/R$  of 50 that is higher than that of the existing Ag nanoparticles/nanowires-based nanocomposites, and many composites using CNF, graphene, and conducting polymers due to the flower-shaped Ag<sub>2</sub>O. The IP/0.3-based IPC displayed very high values of  $\Delta R/R$  of 50, 10, and 3.5 after attaching IPCs on the wrist movement of  $50^{\circ}$ , finger movement of  $180^{\circ}$ , and chin movement respectively. The IP/0.3-based IPC recorded a prominent reduction of TDS from sewage water from 3405 ppm to 1035 ppm and increased the DO levels in the sewage water from 1.3 mg/l to 3.8 mg/l, confirming enhanced aerobic conditions post-treatment with the Ag<sub>2</sub>O-based IPC. The IP/0.3-based IPC shows the highest phosphate removal (88.92 %) from sewage water as compared to other IPCs because of large pores found on the surface The high-performance wearable sensing and large reduction of TDS from sewage water using Ag<sub>2</sub>O-based IPC was due to the production of flower shaped Ag<sub>2</sub>O crystals in the pores of IPC that improved the high reactivity of the Ag<sub>2</sub>O-based IPC.

#### CRediT authorship contribution statement

Priya Khanduri: Writing – original draft, Visualization, Validation, Methodology, Investigation, Data curation, Conceptualization. Varij Panwar: Writing – review & editing, Writing – original draft, Visualization, Validation, Supervision, Investigation, Funding acquisition, Conceptualization. Pradeep Kumar Sharma: Writing – review & editing, Visualization, Conceptualization. Gopinathan Anoop: Writing – review & editing, Visualization, Methodology, Conceptualization. Sanjeev Kumar: Writing – review & editing. Sukho Park: Writing – review & editing, Funding acquisition, Conceptualization.

## Declaration of competing interest

The authors declare that they have no known competing financialinterests or personal relationships that could have appeared to influence the work reported in this paper.

## Acknowledgements

Varij Panwar wishes to thank the Science and Engineering Research Board (SERB) [ECR/2016/001113] for financial help and Graphic Era (Deemed to be University) for providing the final support for this research. Sukho Park wishes to thank the support of the DGIST R&D Program of the Ministry of Science and ICT (23-PCOE-02).

### Supplementary materials

Supplementary material associated with this article can be found, in the online version, at doi:10.1016/j.ceja.2024.100651.

## Data availability

Data will be made available on request.

## References

- C. Lu, X. Zhang, Ionic polymer-metal composites: from material engineering to flexible applications, Acc. Chem. Res. 57 (2024) 131–139, https://doi.org/ 10.1021/acs.accounts.3c00591.
- [2] S. Na, J. Yeom, Y. Chang, Y. Kwon, C. Park, Y.E. Shin, Y.J. Park, H. Ko, Stretchable skin hydration sensor based on hygroscopic and ion conductive polymer composites, Chem. Eng. J. (2023) 455, https://doi.org/10.1016/j. cei.2022.140957.
- [3] S. Ma, Y. Zhang, Y. Liang, L. Ren, W. Tian, L. Ren, High-performance ionic-polymer—metal composite: toward large-deformation fast-response artificial

- muscles, Adv. Funct. Mater. 30 (2020) 1908508, https://doi.org/10.1002/adfm.201908508.
- [4] V. Panwar, P. Khanduri, M.U. Ansari, G. Anoop, S. Park, P(VDF-TrFE)\_PVP\_ionic liquid-based piezo-ionic polymer blend for touch sensing applications, Sensors Actuators A Phys 362 (2023), https://doi.org/10.1016/j.sna.2023.114680.
- [5] J. Lee, M.W.M. Tan, K. Parida, G. Thangavel, S.A. Park, T. Park, P.S. Lee, Water-processable, stretchable, self-healable, thermally stable, and transparent ionic conductors for actuators and sensors, Adv. Mater. 32 (2020) 1–10, https://doi.org/10.1002/adma.201906679.
- [6] M. Amjadi, K. Kyung, I. Park, M. Sitti, Stretchable, skin-mountable, and wearable strain sensors and their potential applications: a review, (2016) 1678–1698. https://doi.org/10.1002/adfm.201504755.
- [7] Y. Li, W. Chen, L. Lu, Wearable and Biodegradable Sensors for Human Health Monitoring, ACS Appl. Bio Mater. 4 (2021) 122–139, https://doi.org/10.1021/ acsabm 0r00859
- [8] Y. Wada, M. Flörke, N. Hanasaki, S. Eisner, G. Fischer, S. Tramberend, M.T.H.van Vliet Satoh, P. Yillia, C. Ringler, P. Burek, D. Wiberg, Modeling global water use for the 21st century: the Water Futures and Solutions (WFaS) initiative and its approaches, Geosci. Model Dev. 9 (2016) 175–222. http://www.geosci-model-dev.net/9/175/2016/gmd-9-175-2016.pdf.
- [9] Y. Wada, D. Wisser, M.F.P. Bierkens, Global modeling of withdrawal, allocation and consumptive use of surface water and groundwater resources, Earth Syst. Dyn. 5 (2014) 15–40, https://doi.org/10.5194/esd-5-15-2014.
- [10] FAO, Coping with water scarcity An action framework for agriculture and food security, 2012.
- [11] F. Dolan, J. Lamontagne, R. Link, M. Hejazi, P. Reed, J. Edmonds, Evaluating the economic impact of water scarcity in a changing world, Nat. Commun. (2021) 12, https://doi.org/10.1038/s41467-021-22194-0.
- [12] P. Jeyakumar, C. Debnath, R. Vijayaraghavan, M. Muthuraj, Purifying surface waters contaminated with natural organic matters and bacteria using Ag/PDAcoated PES membranes, Environ. Eng. Res. 28 (2023) 1–23, https://doi.org/ 10.4491/epr.2022.097.
- [13] M.M. Armendáriz-Ontiveros, Y. Villegas-Peralta, J.E. Madueño-Moreno, J. Álvarez-Sánchez, G.E. Dévora-Isiordia, R.G. Sánchez-Duarte, T.J. Madera-Santana, Modification of thin film composite membrane by chitosan–silver particles to improve desalination and anti-biofouling performance, Membranes (Basel) 12 (2022), https://doi.org/10.3390/membranes12090851.
- [14] X. Chen, A. Yusuf, J.S. del Rio, D.Y. Wang, A facile and robust route to polyvinyl alcohol-based triboelectric nanogenerator containing flame-retardant polyelectrolyte with improved output performance and fire safety, Nano Energy 81 (2021). https://doi.org/10.1016/j.nanoep.2020.105656.
- (2021), https://doi.org/10.1016/j.nanoen.2020.105656.
   [15] M.A. Abu-Saied, E.A. Soliman, K.M. Abualnaj, E.E. Desouky, Highly Conductive Polyelectrolyte Membranes Poly(Vinyl Alcohol)/Poly(2-Acrylamido-2-Methyl Propane Sulfonic acid) (PVA/PAMPS) For Fuel Cell Application, Polymers (Basel), 2021, https://doi.org/10.3390/polym13162638.
- [16] A. Mehmood, N.M. Mubarak, M. Khalid, P. Jagadish, R. Walvekar, E.C. Abdullah, Graphene/PVA buckypaper for strain sensing application, Sci. Rep. (2020), https://doi.org/10.1038/s41598-020-77139-2
- [17] I.A. Pavel, S. Lakard, B. Lakard, Flexible Sensors Based on Conductive Polymers, Chemosensors 10 (2022), https://doi.org/10.3390/chemosensors10030097.
- [18] A. Patel, V. Panwar, Analysis of organic polymer based PVA/CNF membranes, Mater, Today Proc. 64 (2022) 611–614, https://doi.org/10.1016/j. mater. 2022.05.142.
- [19] Y. Guo, H. Xi, Z. Gu, M. Li, X. Li, D. Gao, A self-powered PVA-based flexible humidity sensor with humidity-related voltage output for multifunctional applications, Colloids Surfaces A Physicochem. Eng. Asp. (2023) 658, https://doi. org/10.1016/j.colsurfa.2022.130700.
- [20] B. Prasad, F.S. Gill, V. Panwar, G. Anoop, Development of strain sensor using conductive poly(vinylidene fluoride) (PVDF) nanocomposite membrane reinforced with ionic liquid (IL) & carbon nanofiber (CNF), Compos. Part B Eng. 173 (2019) 106990, https://doi.org/10.1016/j.compositesb.2019.106990.
- [21] V. Panwar, K. Cha, J.O. Park, S. Park, High actuation response of PVDF/PVP/PSSA based ionic polymer metal composites actuator, Sensors Actuators, B Chem 161 (2012) 460–470, https://doi.org/10.1016/j.snb.2011.10.062.
- [22] R. Huang, R. Xu, J. Zhang, J. Wang, T. Zhou, M. Liu, Z. Wang, PVDF-HFP-SN-based gel polymer electrolyte for high-performance lithium-ion batteries, Nano Res. 16 (2023) 9480–9487, https://doi.org/10.1007/s12274-023-5707-x.
- [23] Y. Wei, W. Chen, X. Ge, J. Liang, Z. Xing, Q. Zhang, Z.X. Wang, A flexible, highly conductive, tough ionogel electrolyte containing LiTFSI salt and ionic liquid [EMIM][TFSI] based on PVDF-HFP for high-performance supercapacitors, Polymer (Guildf) 289 (2023), https://doi.org/10.1016/j.polymer.2023.126501.
- [24] B. Prasad, F.S. Gill, V. Panwar, Piezoresistive strain sensing behavior of flexible conductive microporous membrane using acidic ionic liquid, J. Mol. Liq. (2020) 319, https://doi.org/10.1016/j.molliq.2020.114309.
- [25] A.S. Colburn, N. Meeks, S.T. Weinman, D. Bhattacharyya, High total dissolved solids water treatment by charged nanofiltration membranes relating to power plant applications, Ind. Eng. Chem. Res. 55 (2016) 4089–4097, https://doi.org/ 10.1021/acs.ierr.6b00098
- [26] M.A. Ashraf, M.J. Maah, A.K. Qureshi, M. Gharibreza, I. Yusoff, Synthetic polymer composite membrane for the desalination of saline water, Desalin. Water Treat. 51 (2013) 3650–3661, https://doi.org/10.1080/19443994.2012.751152.
- [27] F. Gholami, G. Ghanizadeh, A.A. Zinatizadeh, S. Zinadini, H. Masoumbeigi, Arsenic and total dissolved solids removal using antibacterial/antifouling nanofiltration membranes modified by functionalized graphene oxide and copper ferrodioxide, Water Environ. Res. (2023) 95, https://doi.org/10.1002/wer.10902.

- [28] G. Moradi, S. Zinadini, M. Rahimi, Designing of the green γ-AlOOH@Naringin thin film composite PVDF based nanofiltration membrane and application for pharmaceutical wastewater treatment, J. Environ. Chem. Eng. (2023) 11, https:// doi.org/10.1016/j.jece.2023.109952.
- [29] J.M. Aidong Qiu, Peilin Li, Zhaokun Yang, Yu Yao, Ivan Lee, A path beyond metal and silicon:polymer/nanomaterial composites for stretchable strain sensors, Adv. Funct. Mater. (2019) 29, https://doi.org/10.1002/adfm.201806306.
- [30] Y. Jia, R. Sun, Y. Pan, X. Wang, Z. Zhai, Z. Min, G. Zheng, C. Liu, C. Shen, X. Liu, Flexible and thin multifunctional waterborne polyurethane/Ag film for highefficiency electromagnetic interference shielding, electro-thermal and strain sensing performances, Compos. Part B Eng. 210 (2021) 108668, https://doi.org/ 10.1016/j.compositesb.2021.108668.
- [31] G.W. Huang, H.M. Xiao, S.Y. Fu, Wearable electronics of silver-nanowire/Poly (dimethylsiloxane) nanocomposite for smart clothing, Sci. Rep. 5 (2015) 1–9, https://doi.org/10.1038/srep13971.
- [32] P.W. Bohn, M. Elimelech, J.G. Georgiadis, B.J. Mariñas, A.M. Mayes, A.M. Mayes, Science and technology for water purification in the coming decades, Nature 452 (2009) 337–346, https://doi.org/10.1142/9789814287005 0035.
- [33] Y. Ying, W. Ying, Q. Li, D. Meng, G. Ren, R. Yan, X. Peng, Recent advances of nanomaterial-based membrane for water purification, Appl. Mater. Today. 7 (2017) 144–158, https://doi.org/10.1016/j.apmt.2017.02.010.
- [34] J. Kim, B. Van Der Bruggen, The use of nanoparticles in polymeric and ceramic membrane structures: Review of manufacturing procedures and performance improvement for water treatment, Environ. Pollut. 158 (2010) 2335–2349, https://doi.org/10.1016/j.envpol.2010.03.024.
- [35] A.A. Yaqoob, K. Umar, M.N.M. Ibrahim, Silver nanoparticles: various methods of synthesis, size affecting factors and their potential applications—a review, Appl. Nanosci. 10 (2020) 1369–1378, https://doi.org/10.1007/s13204-020-01318-w.
- [36] N. Ally, B. Gumbi, A review on metal nanoparticles as nano-sensors for environmental detection of emerging contaminants, Mater. Today Proc (2023), https://doi.org/10.1016/j.matpr.2023.08.032.
- [37] F.A. Samhan, N. Ismail, F.A. Samhan, N. Ismail, Synergistic role of Ag nanoparticles and Cu nanorods dispersed on graphene on membrane desalination and biofouling, J. Ind. Eng. Chem. 65 (2018) 127–136, https://doi.org/10.1016/j. ijec.2018.04.021.
- [38] L. Huang, S. Zhao, Z. Wang, J. Wu, J. Wang, S. Wang, In situ immobilization of silver nanoparticles for improving permeability, antifouling and anti-bacterial properties of ultrafiltration membrane, J. Memb. Sci. 499 (2016) 269–281, https:// doi.org/10.1016/j.memsci.2015.10.055.
- [39] H.S. Barud, C. Barrios, T. Regiani, R.F.C. Marques, M. Verelst, J. Dexpert-Ghys, Y. Messaddeq, S.J.L. Ribeiro, Self-supported silver nanoparticles containing bacterial cellulose membranes, Mater. Sci. Eng. C. 28 (2008) 515–518, https://doi. org/10.1016/j.msec.2007.05.001.
- [40] V. Panwar, A. Gopinathan, Ionic polymer-metal nanocomposite sensor using the direct attachment of acidic ionic liquid in a polymer blend, J. Mater. Chem. C. (2019). https://doi.org/10.1039/COTC02355K.
- [41] V. Panwar, S. Mohanty, G. Anoop, S. Kumar, Actuation and self-sensing performance of soft polymer actuator skin using polyelectrolyte attached terpolymer, Sensors Actuators, A Phys 315 (2020) 112277, https://doi.org/ 10.1016/j.spa.2020.112277
- [42] A. Al-Sarraj, K.M. Saoud, A. Elmel, S. Mansour, Y. Haik, Optoelectronic properties of highly porous silver oxide thin film, SN Appl. Sci. 3 (2021) 1–13, https://doi. org/10.1007/s42452-020-04091-1.
- [43] Z.H. Dhoondia, H. Chakraborty, Lactobacillus mediated synthesis of silver oxide nanoparticles, Nanomater. Nanotechnol. 2 (2012), https://doi.org/10.5772/ 55741
- [44] S. Satapathy, P.K. Gupta, S. Pawar, K.B.R. Varma, Crystallization of Beta-phase Poly (vinylidene fluoride) films using dimethyl sulfoxide (DMSO) solvent and at suitable annealing condition, Mater. Sci. (2008) 1–18. http://arxiv.org/abs/ 0808 0419
- [45] K. Richter, P.S. Campbell, T. Baecker, A. Schimitzek, Ionic liquids for the synthesis of metal nanoparticles, 13 (2013) 1–13. https://doi.org/10.1002/pssb.201248547.
- [46] S. Elyamny, M. Eltarahony, M.A. Serie, M.M. Nabil, One pot fabrication of Ag @ Ag 2 O core shell nanostructures for biosafe antimicrobial and antibiofilm applications, Sci. Rep. (2021) 1–13, https://doi.org/10.1038/s41598-021-01687-
- [47] W.M. Shume, H.C.A. Murthy, E.A. Zereffa, A review on synthesis and characterization of Ag<sub>2</sub>O nanoparticles for photocatalytic applications, J. Chem. 2020 (2020) 5039479, https://doi.org/10.1155/2020/5039479.
- [48] O. Pawar, N. Deshpande, S. Dagade, S. Waghmode, P.Nigam Joshi, Green synthesis of silver nanoparticles from purple acid phosphatase apoenzyme isolated from a new source Limonia acidissima, J. Exp. Nanosci. 11 (2016) 28–37, https://doi.org/ 10.1080/17458080.2015.1025300.
- [49] O. Pawar, N. Deshpande, S. Dagade, S. Waghmode, P.Nigam Joshi, Green synthesis of silver nanoparticles from purple acid phosphatase apoenzyme isolated from a new source Limonia acidissima, J. Exp. Nanosci. 11 (2016) 28–37, https://doi.org/ 10.1080/17458080.2015.1025300.
- [50] L.M. Fu, J.H. Hsu, M.K. Shih, C.W. Hsieh, W.J. Ju, Y.W. Chen, B.H. Lee, C.Y. Hou, Process optimization of silver nanoparticle synthesis and its application in mercury detection, Micromachines (2021) 12, https://doi.org/10.3390/mi12091123.
- [51] L.S. Panwar, V. Panwar, G. Anoop, S. Park, Carbon nanofiber-polyelectrolyte triggered piezoelectric polymer-based hydrophilic nanocomposite for high sensing voltage generation, J. Mater. Res. Technol. 17 (2022) 3246–3261, https://doi.org/ 10.1016/j.jmrt.2022.02.075.

- [52] L. Ruan, X. Yao, Y. Chang, L. Zhou, G. Qin, X. Zhang, Properties and applications of the β phase poly(vinylidene fluoride), Polymers (Basel) 10 (2018), https://doi.org/ 10.3390/polym10030228
- [53] B. Khodashenas, H.R. Ghorbani, Synthesis of silver nanoparticles with diff erent shapes, (2019) 1823–1838.
- [54] G.G. Tsutsumanova, N.D. Todorov, S.C. Russev, M. V Abrashev, V.G. Ivanov, A. V Lukoyanov, Silver Flowerlike Structures for Surface-Enhanced Raman Spectroscopy, (2021).
- [55] M.S. Cetin, H.A. Karahan Toprakci, Flexible electronics from hybrid nanocomposites and their application as piezoresistive strain sensors, Compos. Part B Eng. 224 (2021) 109199, https://doi.org/10.1016/j.compositesb.2021.109199.
- [56] V. Panwar, G. Anoop, M. Sharma, S.S. Gaur, S. Park, Sugarcane liquid-generated silver nanoparticles connected ionic polymer nanocomposite for enhanced electrical and wearable sensing signals, Mater. Today Chem. 26 (2022) 101195, https://doi.org/10.1016/j.mtchem.2022.101195.
- [57] B. Prasad, F.S. Gill, V. Panwar, G. Anoop, Development of strain sensor using conductive poly(vinylidene fluoride) (PVDF) nanocomposite membrane reinforced with ionic liquid (IL) & carbon nanofiber (CNF), Compos. Part B Eng. 173 (2019) 106990, https://doi.org/10.1016/j.compositesb.2019.106990.
- [58] X.L. Yunpeng Jia, Ruizhou Sun, Yamin Pan, Xin Wang, Zhanyu Zhai, Zhiyu Min, Guoqiang Zheng, Chuntai Liu, Changyu Shen, Flexible and thin multifunctional waterborne polyurethane/Ag film for high-efficiency electromagnetic interference shielding, electro-thermal and strain sensing performances, Compos. Part B Eng. (2021) 210, https://doi.org/10.1016/j.compositesb.2021.108668.
- [59] N. Liu, G. Fang, J. Wan, H. Zhou, H. Long, X. Zhao, PEDOT Electrospun, PSS-PVA nanofiber based ultrahigh-strain sensors with controllable electrical conductivity, J. Mater. Chem. 21 (2011) 18962–18966, https://doi.org/10.1039/c1jm14491j.
- [60] Y. Wang, H. Mi, Q. Zheng, H. Zhang, Z. Ma, S. Gong, Highly stretchable and sensitive piezoresistive carbon nanotube/elastomeric triisocyanate-crosslinked polytetrahydrofuran nanocomposites, J. Mater. Chem. C. 4 (2016) 460–467, https://doi.org/10.1039/C5TC03413B.
- [61] P. Costa, S. Gonçalves, H. Mora, S.A.C. Carabineiro, J.C. Viana, S. Lanceros-Mendez, Highly Sensitive Piezoresistive Graphene-Based Stretchable Composites for Sensing Applications, ACS Appl. Mater. Interfaces. 11 (2019) 46286–46295, https://doi.org/10.1021/acsami.9b19294.
- [62] S. Zhang, H. Liu, S. Yang, X. Shi, D. Zhang, C. Shan, L. Mi, C. Liu, C. Shen, Z. Guo, Ultrasensitive and highly compressible piezoresistive sensor based on polyurethane sponge coated with a cracked cellulose nanofibril/silver nanowire layer, ACS Appl. Mater. Interfaces. 11 (2019) 10922–10932, https://doi.org/10.1021/ acsami.9b00900.
- [63] S. Yoon, Y.J. Kim, Y.R. Lee, N.-E. Lee, Y. Won, S. Gandla, S. Kim, H.-K. Kim, Highly stretchable metal-polymer hybrid conductors for wearable and self-cleaning sensors, NPG Asia Mater 13 (2021) 4, https://doi.org/10.1038/s41427-020-00277-6.
- [64] Z. Wang, Y. Liu, D. Zhang, C. Gao, Y. Wu, Mussel-inspired self-healing PDMS/ AgNPs conductive elastomer with tunable mechanical properties and efficient antibacterial performances for wearable sensor, Compos. Part B Eng. 224 (2021) 109213, https://doi.org/10.1016/j.compositesb.2021.109213.
- [65] A.A. Lagum, Simultaneous nitrification and denitrification by controlling current density and dissolved oxygen supply in a novel electrically-induced membrane

- bioreactor, J. Environ. Manage. (2022) 322, https://doi.org/10.1016/j.ienvman 2022 116131
- [66] Q.F. Alsalhy, F.H. Al-Ani, A.E. Al-Najar, A new Sponge-GAC-Sponge membrane module for submerged membrane bioreactor use in hospital wastewater treatment, Biochem. Eng. J. 133 (2018) 130–139, https://doi.org/10.1016/j.bej.2018.02.007.
- [67] Y. Zhou, M.N. Anwar, B. Guo, W. Huang, Y. Liu, Response of antibiotic resistance genes and microbial niches to dissolved oxygen in an oxygen-based membrane biofilm reactor during greywater treatment, Sci. Total Environ. 833 (2022), https://doi.org/10.1016/j.scitotenv.2022.155062.
- [68] Z.J. Feng, M. Wu, M.X. Sun, H.Y. Liu, Y.Z. Zhang, J. Dai, The effects of different carriers on removal performance and membrane fouling by HMBR in treating sewage with low carbon-to-nitrogen ratio, Process Saf. Environ. Prot. 102 (2016) 768–776, https://doi.org/10.1016/j.psep.2016.06.019.
- [69] K.V. Reddy, A. Vamshi, K. Reddy, B. Suresh Babu, T.V. Lakshmi, Applications of bacillus sp in aquaculture waste water treatment, Int. J. Sci. Res. Sci. Technol. 5 (2018) 1806–1812. www.ijsrst.com.
- [70] G. Jing, X. Wang, H. Zhao, Study on TDS removal from polymer-flooding wastewater in crude oil: extraction by electrodialysis, Desalination 244 (2009) 90–96, https://doi.org/10.1016/j.desal.2008.04.039.
- [71] I. Purnawan, D. Angputra, S.C. Debora, E.F. Karamah, A. Febriasari, S. Kartohardjono, Polyvinylidene fluoride membrane with a polyvinylpyrrolidone additive for tofu industrial wastewater treatment in combination with the coagulation-flocculation process, Membranes (Basel) 11 (2021), https://doi.org/ 10.3390/membranes11120948.
- [72] P. Xu, J.E. Drewes, D. Heil, Beneficial use of co-produced water through membrane treatment: technical-economic assessment, Desalination 225 (2008) 139–155, https://doi.org/10.1016/j.desal.2007.04.093.
- [73] Z. Anari, A. Sengupta, K. Sardari, S.R. Wickramasinghe, Surface modification of PVDF membranes for treating produced waters by direct contact membrane distillation, Sep. Purif. Technol. 224 (2019) 388–396, https://doi.org/10.1016/j. seppur.2019.05.032.
- [74] R. Shang, A.R.D. Verliefde, J. Hu, S.G.J. Heijman, L.C. Rietveld, The impact of EfOM, NOM and cations on phosphate rejection by tight ceramic ultrafiltration, Sep. Purif. Technol. 132 (2014) 289–294, https://doi.org/10.1016/j. seppur.2014.05.024.
- [75] S. Tang, J. Li, Z. Zhang, B. Ren, X. Zhang, Comparison of long-term ceramic membrane bioreactors without and with in-situ ozonation in wastewater treatment: Membrane fouling, effluent quality and microbial community, Sci. Total Environ. 652 (2019) 788–799, https://doi.org/10.1016/j.scitotenv.2018.10.284.
- [76] A. Zhang, S. Fang, H. Xi, J. Huang, Y. Li, G. Ma, J. Zhang, Highly efficient and selective removal of phosphate from wastewater of sea cucumber aquaculture for microalgae culture using a new adsorption-membrane separation-coordinated strategy, Front. Environ. Sci. Eng. (2023) 17, https://doi.org/10.1007/s11783-023-1720-2
- [77] J.I. Lee, J.S. Oh, S.C. Yoo, E.H. Jho, C.G. Lee, S.J. Park, Removal of phosphorus from water using calcium-rich organic waste and its potential as a fertilizer for rice growth, J. Environ. Chem. Eng. (2022) 10, https://doi.org/10.1016/j. iece 2022 107367
- [78] M.T. Gutierrez-Wing, R.F. Malone, K.A. Rusch, Evaluation of polyhydroxybutyrate as a carbon source for recirculating aquaculture water denitrification, Aquac. Eng. 51 (2012) 36–43, https://doi.org/10.1016/j.aquaeng.2012.07.002.